Journal of Power Sources 202 (2012) 157–165

Contents lists available at SciVerse ScienceDirect

Journal of Power Sources

journal homepage: www.elsevier.com/locate/jpowsour

Thermodynamic analysis of ammonia-fed solid oxide fuel cells

F. Ishak, I. Dincer, C. Zamfirescu *

Faculty of Engineering and Applied Science, University of Ontario Institute of Technology, 2000 Simcoe Street North, Oshawa, Ontario, Canada L1H 7K4

ARTICLE INFO

Article history:
Received 27 September 2011
Received in revised form 23 October 2011
Accepted 24 October 2011
Available online 22 November 2011

Keywords:
Ammonia
Dusty gas model
Hydrogen
Solid oxide fuel cell
Performance

ABSTRACT

This paper studies the thermodynamic aspects of direct ammonia-fed solid oxide fuel cells (DA-SOFC). In this regard, anode-supported oxygen ion-conducting solid oxide fuel cells (SOFC–O) and proton-conducting solid oxide fuel cells (SOFC–H) fuelled with ammonia are compared on the basis of their thermodynamic and electrochemical performances at open and closed circuit conditions. Based on the thermodynamic equilibrium, full conversion of ammonia is attained at a temperature of 700 K and atmospheric pressure. From the results of this study, it is found that the overall performance of the fuel cell is largely dependent on critical factors such as the operating temperature and the properties of the electrolyte and electrodes layers. On average, the peak power density of ammonia-fed SOFC–H is 20–30% higher than its SOFC–O counterpart under most examined conditions. This is mainly attributed to the higher concentration of hydrogen at the anode of SOFC–H in all cases.

1. Introduction

Trade market fluctuations and periodic economic cycles like the recent global economic recession of 2008 have a significant near-term impact on the world energy demand. From a long-term perspective, there is no doubt that the continuous growth of the world population presents great challenges to energy resources and development. Therefore, it is evident that there is an ever growing need for sustainable and environmentally benign energy supply as well as efficient power production and distribution.

Fuel cells have been identified as a promising technology of power production for stationary and mobile applications due to their high efficiency and small environmental footprint. As such, substantial research and development efforts are invested in advancing this technology. In particular, solid oxide fuel cells remain at the forefront of this focus due to several advantages like the capability of directly operating on renewable and non-renewable energy carriers and fuels.

As the reserve of non-renewable resources depletes over time, hydrogen is expected to emerge and attain a major market share as a renewable energy carrier. The shift of energy paradigm initiated by the new hydrogen economy is expected to have a dramatic impact on the environmental and economic sustainability of societies around the world. However, this progress is hindered by technical and economic challenges that must be overcome before the transition is realized. To that extent, research communities have started investigating the use of suitable intermediate hydrogen carriers in effort to eliminate these challenges and shortcomings.

The task of identifying the optimal hydrogen carrier is not trivial as it involves multi-criteria decision making and consideration of various technical and economic aspects like safety, energy density and cost of processing or recycling. This has led to the careful scrutiny of diverse spectrum of storage materials like metal hydrides, metal-organic framework and amide systems. Despite extensive research and development efforts, these materials and compounds have major drawbacks revolving around the rate of hydrogen desorption, recyclability and high cost [1,2]. In this regard, anhydrous ammonia can potentially eliminate the need for complex and perilous hydrogen storage systems.

Limited attention has been given to the analysis of ammonia-fed solid oxide fuel cells. For instance, Ni et al. [3] compared the thermodynamic performance of ammonia-fed oxygen ion-conducting (SOFC–O) and proton-conducting (SOFC–H) solid oxide fuel cells operating under temperatures between 873 K and 1273 K. The study also assumed an indirect reaction mechanism whereby ammonia was first decomposed to nitrogen and hydrogen while the latter was oxidized to produce electric power. Comparison of the cell potential of both types of fuel cells over a wide range of fuel and oxidant utilizations signified the superiority of SOFC–H mainly due to the absence of water vapour formation and higher partial pressure of hydrogen at the anode. The maximum theoretical (electrochemical) efficiency was found to increase with increasing fuel utilization which is consistent with thermodynamic studies on the hydrogen-fed solid oxide fuel cells as given, for example, by Demin and Tsiakaras [4].

Ni et al. [5] also used an electrochemical macro-model to compare the operating voltage and power density of ammonia-fed

* Corresponding author. Tel.: +1 9059224455; fax: +1 9057213370.
E-mail addresses: fadi.ishak@uoit.ca (F. Ishak), ibrahim.dincer@uoit.ca (I. Dincer), calin.zamfirescu@uoit.ca, calinzam@gmail.com (C. Zamfirescu).

0378-7753/$ – see front matter © 2011 Elsevier B.V. All rights reserved.
doi:10.1016/j.jpowsour.2011.10.142

Nomenclature

B_0	permeability [m^2]
dx	depth of electrode layer [m]
D^{eff}	effective binary diffusion [$m^2\ s^{-1}$]
D_k^{eff}	effective Knudsen diffusion [$m^2\ s^{-1}$]
E	reversible cell potential or voltage [V]
E^0	standard cell potential or voltage [V]
f	fugacity of chemical species in the system
f^0	fugacity of chemical species at STP
F	Faraday's constant (96485 C mol^{-1})
$\overline{g}$	specific molar Gibbs energy [J mol^{-1}]
G	Gibbs energy [J]
$\overline{g}^0$	specific molar Gibbs energy at STP [J mol^{-1}]
J	current density [A m^{-2}]
J_0	exchange current density [A m^{-2}]
M	molar mass [g mol^{-1}]
n	number of moles [mol]
N	molar flux [mol $m^{-2}\ s^{-1}$]
p	partial pressure [kPa]
P	pressure, total pressure [kPa]
r_p	mean pore radius of electrode [m]
R	gas constant [J $mol^{-1}\ K^{-1}$]
R_Ω	electrolyte resistivity [Ω m]
T	temperature [K]
U	utilization [%]
V	working potential or voltage [V]
y	molar fraction of chemical species
z	number of electrons transferred per mole of fuel

Greek letters

α	charge transfer coefficient
Γ	dimensionless temperature
δ	electrolyte thickness [m]
Δ	net change of quantity
ε	porosity of electrode
ε/κ	Lennard–Jones temperature parameter [K]
μ	viscosity [N s m^{-2}]
σ	molecular collision diameter [Å]
τ	tortuosity of electrode
$\varphi_{act,an}$	anode activation over-potential [V]
$\varphi_{act,ca}$	cathode activation over-potential [V]
$\varphi_{conc,an}$	anode concentration over-potential [V]
$\varphi_{conc,ca}$	cathode concentration over-potential [V]
φ_Ω	ohmic over-potential of electrolyte [V]
Ω_D	collision integral of diffusion

Subscripts

eff	effective
f	fuel
i, j	chemical species
k	Knudsen diffusion
o	oxidant
T	temperature
P	pressure

Acronyms

BCNO	Barium cerate neodymium oxide
BCSm	Barium cerate samarium oxide
DA-SOFC	Direct ammonia solid oxide fuel cell
DeNOx	Denitrification (nitrous oxides)
DGM	Dusty gas model
GEM	Gibbs energy minimization
LHV	Lower heating value
LSM-YSZ	Lanthanum strontium manganite/yttria-stabilized zirconia
Ni-YSZ	Nickel/yttria-stabilized zirconia
OCV	Open cell voltage
SOFC–H	Hydrogen proton (H^+) conducting solid oxide fuel cell
SOFC–O	Oxygen ion (O^{2-}) conducting solid oxide fuel cell
STP	Standard temperature and pressure
TPB	Triple-phase boundary
YSZ	Yttria-stabilized zirconia

SOFC–O and SOFC–H at a temperature of 1073 K and atmospheric pressure only. The anode-supported fuel cells were based on yttria-stabilized zirconia (YSZ) and barium cerate samarium oxide (BCSm) electrolytes for SOFC–O and SOFC–H, respectively. The analysis assumed a leak-free construction, negligible interfacial resistance, no fuel cross-over or electronic conductivity through the electrolyte layer. Thus only activation, ohmic and concentration over-potentials were addressed. Their work also emphasized the higher performance of SOFC–O over SOFC–H. This was explained by the high ohmic over-potential of BCSm electrolyte and the high concentration over-potential at the SOFC–H cathode as the water vapour formation obstructed the oxygen transport to the reaction sites. The results were quite different from those presented by Assabumrungrat et al. [6] and Biesheuvel and Geerlings [7] who advocated the superior performance of SOFC–H in comparison to SOFC–O using methanol and methane fuels at the same operating conditions.

With the focus on SOFC–H, another study was conducted by Ni et al. [8] to examine the impact of different types of structural support on the performance of the fuel cell. It was found that higher power density can be achieved by the anode-supported cell primarily because of the thinner electrolyte material which greatly reduced the ohmic polarization. Later, their electrochemical model was improved [9] by incorporating a first-order model of the kinetic rate of ammonia decomposition which was previously developed by Chellappa et al. [10]. The kinetic model was coupled with the dusty gas model (DGM) to obtain the molar fraction of ammonia across the anode thickness at various temperatures. The model showed that the ammonia was fully decomposed at an approximate anode depth of 25 μm and 300 μm at 1073 K and 873 K, respectively. It was also shown that ammonia did not fully decompose at temperatures below 873 K which resulted in a low-partial pressure of hydrogen and deteriorated performance of the fuel cell.

This study is motivated by the technical challenges to the rapid development of hydrogen markets and infrastructure which include the constraints of safe transportation, low temperature storage as well as the high pressure necessary to achieve the required energy density. The objective of this paper is to highlight the advantages and merits of ammonia as an energy carrier by shedding light on various important aspects like its energy storage capacity as well as its demand and supply around the world. Furthermore, the aim of this work is to examine the operating principles of ammonia-fed solid oxide fuel cells and investigate the cell-level thermodynamic and electrochemical performances at open and closed circuit conditions.

2. Ammonia as a hydrogen carrier

Ammonia is extensively used in many industries including refrigeration, petrochemical and food processing. Furthermore, large quantities of ammonia are used worldwide for agricultural purposes. It is estimated that the global capacity of ammonia

Table 1
Comparison of energy storage capacity.

Energy carrier	Density ($g\,L^{-1}$)	Fraction of hydrogen (% H_2)	Volumetric density ($gH_2\,L^{-1}$)	Energy density ($MJ\,L^{-1}$)
Gaseous H_2 (298 K, 10 MPa)	7.68	100	7.7	0.92
Liquid H_2 (20 K, 0.1 MPa)	71.28	100	71.3	8.56
Liquid NH_3 (298 K, 1 MPa)	603	17.76	107.1	12.85

Sources: [15,16].
Energy density is based on LHV of hydrogen.

production was about 153 million tonnes in 2009 and is expected to increase to 244 million tonnes by 2014 [11]. This major increase is, in part, due to the growing use of ammonia in emerging emission control ($DeNO_x$) technologies in industrial and automotive applications.

The infrastructure and technology of ammonia production are also well established with existing industrial plants around the world to support the increasing demand for ammonia. Steam reforming of natural gas is the current primary method of ammonia production. Consequently, the best available technologies emits about 1.7 tonnes of carbon dioxide per tonne of ammonia production most of which can be easily recovered for use in downstream processes such as the production of urea or other derivatives [12]. This figure excludes the potential amount of carbon dioxide emitted when carbon-based fuel is used to provide the motive power to the process of ammonia production.

Recently, ammonia has been heralded as an excellent hydrogen carrier for its several favourable attributes. For example, it can be liquefied at ambient temperature under a moderate pressure of 1.0 MPa for the purpose of storage and transportation. As shown in Table 1, its energy density is 48% higher than that of liquefied hydrogen. The gravimetric and volumetric capacities of ammonia also exceed the ultimate target for hydrogen storage capacity set by the US Department of Energy [13]. Furthermore, ammonia leakage is easily detectable at concentrations as low as 17 ppm [14] due to its pungent odour.

In contrast, the utilization of ammonia in certain applications is hindered by safety implications among other concerns. Ammonia vapour can be toxic and life-threatening at high concentration. It is also known that exposure to the vapour at a concentration of 1700 ppm can cause severe lung damage or respiratory failure and death at 5000 ppm [17]. Another significant concern is the corrosive effects of ammonia on some materials like copper, zinc and their alloys. In order to mitigate these risks and shortcomings, some focus has been directed towards stabilizing the ammonia by combining it in metal ammine complexes [18]. This allows for transportation and long-term storage of ammonia in solid-state form and provides the means of releasing the hydrogen as needed.

3. Analysis

3.1. Thermodynamic equilibrium of ammonia decomposition

When heated, ammonia decomposes to hydrogen and nitrogen according to the following reaction:

$$NH_3 \leftrightarrow \frac{3}{2}H_2 + \frac{1}{2}N_2 \tag{1}$$

The above reaction is endothermic and depends on the temperature and pressure of the system among other factors. The reaction proceeds to the right as the temperature increases or to the left as the pressure increases thus producing less hydrogen. The thermodynamic equilibrium of ammonia can be obtained by minimizing the total Gibbs energy of the reaction:

$$(\Delta G_{system})_{T,P} = 0 \tag{2}$$

where the Gibbs energy of the system can be defined as the summation of the product of moles of chemical species i multiplied by the respective specific Gibbs energy at constant temperature and pressure

$$G_{system} = \Sigma n_i \overline{g}_i \tag{3}$$

The specific Gibbs energy can be described as the sum of the standard Gibbs function of formation and the chemical activity of a given species i. For real gases, the activity of species is defined as the ratio of its fugacity in the system to that at standard temperature and pressure (STP) conditions:

$$\overline{g}_i = \overline{g}_{fi}^0 + RT \ \ln\frac{f_i}{f_i^0} \tag{4}$$

If ideal or perfect gas conditions are assumed, the activity of the gaseous species is equal to its partial pressure in the system. For condensed matter (solid or liquid), the activity is equal to unity. Therefore, the total Gibbs energy of the system is

$$G_{system} = \left(\sum n_i[\overline{g}_{fi}^0 + \overline{R}T \ \ln(y_i P)]\right)_{gas} + \left(\sum n_i \overline{g}_{fi}^0\right)_{condensed} \tag{5}$$

As an advantage of this method, chemical reactions need not to be specified. Instead, Gibbs energy minimization (GEM) requires data of the standard Gibbs function of formation of all chemical species which are expected to be involved or contribute to the thermodynamic equilibrium under consideration.

3.2. Description and operational principles of DA-SOFC

The operating principle of direct ammonia-fed solid oxide fuel cell (DA-SOFC) with oxygen ion conducting electrolyte is assumed to take an indirect path to the oxidation of the fuel by thermally decomposing the ammonia to extract the hydrogen which will be electrochemically oxidized in the fuel cell. Depending on the thermodynamic equilibrium of the ammonia decomposition reaction at given temperature and pressure, nitrogen gas may be produced in high concentration. The inert nitrogen gas can dilute the hydrogen concentration at the anode resulting in reduction of the reversible cell potential. Furthermore, the nitrogen gas produced is discharged from the anode compartment along with other gaseous effluents as depicted in Fig. 1.

On the cathode side, oxygen from air is transported across the cathode layer to the cathode–electrolyte interface where it is reduced to oxygen ion. The oxygen ions are then transported through the electrolyte to electrochemically react with hydrogen

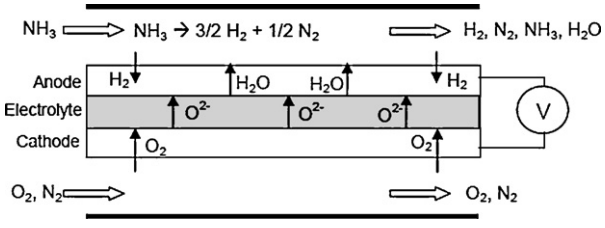

Fig. 1. Schematic representation of oxygen ion-conducting direct ammonia solid oxide fuel cell.

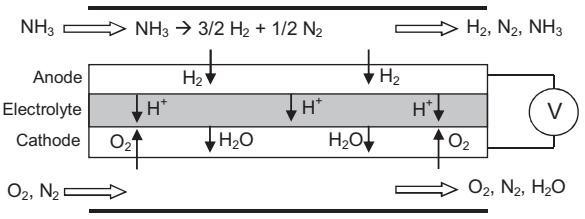

Fig. 2. Schematic representation of proton-conducting direct ammonia solid oxide fuel cell.

at the anode–electrolyte interface. The water vapour produced by the reaction is transported to the anode channel which can also dilute the fuel concentration. The water vapour then exits the cell along with unreacted fuel and other effluents.

Fig. 2 depicts the configuration of direct ammonia-fed solid oxide fuel cell (DA-SOFC) with proton-conducting electrolyte. As ammonia enters the cell at the anode side, it decomposes to hydrogen and nitrogen in proportions governed by the thermodynamic equilibrium at specific temperature and pressure. While nitrogen acts as an inert diluent, hydrogen is transported to the anode–electrolyte interface to be oxidized to hydrogen protons. Subsequently, hydrogen protons are transported through the electrolyte layer to the cathode–electrolyte interface to undergo electrochemical reaction with oxygen from the cathode side. The water vapour produced by the fuel cell reaction is then transferred to the bulk gas in the cathode channel where it exits the cell along with other effluents. This is a major advantage since hydrogen is not diluted by the water vapour generated from the fuel cell reaction.

3.3. Thermodynamic and electrochemical analyses

The equilibrium potential of any fuel cell is affected by the partial pressures of the species involved in the electrochemical reaction. Under open-circuit conditions, the potential (voltage) can be written as

$$E = E^0 + \frac{\bar{R}T}{2F} \ln \left[\frac{p_{H_2} (p_{O_2})^{1/2}}{p_{H_2O}} \right] \tag{6}$$

where

$$E^0 = \frac{-\Delta G}{zF} \tag{7}$$

Furthermore, the examination of the potential of solid oxide fuel cells at closed circuit conditions requires the characterization of the over-potentials affecting the cell operation. The working potential or voltage of SOFC can be characterized as

$$V = E - \varphi_{act,an} - \varphi_{act,ca} - \varphi_{\Omega} - \varphi_{conc,an} - \varphi_{conc,ca} \tag{8}$$

The activation over-potential is an irreversible loss related to the electrode kinetics and represents the difference between the actual potential (closed-circuit conditions) and the reversible potential (open-circuit conditions). The implicit relationship between the current density and the activation over-potential can be described using the Butler–Volmer expression [19]

$$J = J_0 \left[\exp\left(\frac{\alpha z F \varphi_{act}}{\bar{R}T} \right) - \exp\left(-\frac{(1-\alpha) z F \varphi_{act}}{\bar{R}T} \right) \right] \tag{9a}$$

The exchange current density (J_0) is a measure of the magnitude of electron activity at the equilibrium potential of the electrode. Its value is highly influenced by the electrode material, structure and other factors such as the temperature of the reaction and the length of the triple-phase boundary (TPB) [20]. The charge transfer coefficient (α) describes the effect of the electric potential on the ratio of the forward to the reverse activation barrier. For most electrochemical reactions in solid oxide fuel cells, this value is assumed to be 0.5 [21]. As such, the explicit relationship of the activation over-potential is

$$\varphi_{act,\gamma} = \frac{\bar{R}T}{F} \sin \; h^{-1} \left(\frac{J}{z J_{0,\gamma}} \right), \quad \gamma = \text{anode}, \quad \text{cathode} \tag{9b}$$

The electronic resistance of the fuel cell electrode and interconnect is usually very small and is considered negligible when compared to the ionic resistance of the electrolyte. The ionic resistance can be described by Ohm's law [22] as

$$\varphi_{\Omega} = J \delta R_{\Omega} \tag{10}$$

The electrolyte resistance (R_{Ω}) is a function of the electrolyte properties and is highly dependent on the operating temperature.

The concentration over-potential accounts for losses incurred by the resistance of the porous electrode to the transport of gaseous species between the gas channel and the reaction sites at TPB. The mass transport in the electrodes is driven by the diffusion of reacting species due to concentration gradient as well as the permeation caused by the pressure gradient. Several mass transport models with varied accuracies have been used to capture the effects of concentration over-potential on the performance of fuel cells.

It has been demonstrated that the highest accuracy can be achieved using the dusty gas model [23] and the mean transport pore model (MTPM) [24]. In particular, DGM visualizes the porous medium as a collection of large spherical particles suspended in space by external forces. The model takes into account the effects of diffusion and permeation mechanisms on the concentration of reacting species which is essential when modelling pressurized fuel cell systems. The one-dimensional multi-component mass transport DGM can be written as

$$\frac{N_i}{D_{i,k}^{\text{eff}}} + \sum_{j=1, j \neq i} \frac{y_j N_i - y_i N_j}{D_{ij}^{\text{eff}}} = -\frac{1}{\bar{R}T} \left[P \frac{dy_i}{dx} + y_i \frac{dP}{dx} \left(1 + \frac{B_0 P}{\mu_{\text{mix}} D_{i,k}^{\text{eff}}} \right) \right] \tag{11}$$

where the effective Knudsen diffusion accounts for the porosity and tortuosity of the electrode such that [25]:

$$D_{i,k}^{\text{eff}} = \frac{2}{3} \frac{\varepsilon}{\tau} \sqrt{\frac{8\bar{R}T}{\pi M_i}} r_p \tag{12}$$

The effective binary diffusion of chemical species can be obtained using the Chapman–Enskog equation [26]:

$$D_{ij}^{\text{eff}} = 0.0018583 \frac{\varepsilon}{\tau} \sqrt{T^3 \left(\frac{1}{M_i} + \frac{1}{M_j} \right)} \frac{1}{P \sigma_{ij}^2 \Omega_{D,ij}} \tag{13}$$

and the mean characteristic length (σ_{ij}) of the molecular collision diameter of species i and j is given by

$$\sigma_{ij} = \frac{(\sigma_i + \sigma_j)}{2} \tag{14}$$

The collision integral ($\Omega_{D,ij}$) is a function of temperature and the Lennard–Jones parameter (k/ε_{ij}) such that

$$\Omega_{D,ij} = \frac{1.06036}{\Gamma^{0.15610}} + \frac{0.19300}{\exp(0.47635\Gamma)} + \frac{1.03587}{\exp(1.52996\Gamma)} + \frac{1.76474}{\exp(3.89411\Gamma)} \tag{15}$$

where

$$\Gamma = \frac{kT}{\varepsilon_{ij}} \tag{16}$$

and

$$\varepsilon_{ij} = \sqrt{\varepsilon_i \varepsilon_j} \tag{17}$$

The values of the parameters in Eqs. (12)–(17) have been obtained from Refs. [26,27]. The permeability of the porous electrode is estimated using the Kozeny–Carman relationship [28]

$$B_0 = \frac{4\varepsilon^3 r_p^2}{72\tau(1-\varepsilon)^2} \tag{16'}$$

Furthermore, the viscosity of gas mixture can be calculated using the following semi-empirical equation [29]:

$$\mu_{\text{mix}} = \frac{\sum y_i \mu_i \sqrt{M_i}}{\sum y_i \sqrt{M_i}} \tag{17'}$$

The gas viscosities are obtained from Ref. [26]. As presented by Zhu et al. [30], the summation of Eq. (11) allows for the evaluation of the pressure gradient (dP/dx) across the electrode layer as

$$\frac{dP}{dx} = -\frac{\sum_{i=1}(N_i/D_{i,k}^{\text{eff}})}{(1/\bar{R}T) + (B_0 P/\mu \bar{R}T)\sum_{i=1}(y_i/D_{i,k}^{\text{eff}})} \tag{18}$$

At TPB, the molar flux of the gaseous reactants involved in the electrochemical reaction, namely hydrogen and oxygen, can be related to the current density as

$$N_i = \frac{J}{zF} \tag{19}$$

Depending on the type of electrolyte (SOFC–O or SOFC–H), the molar flux of water vapour can be calculated using Graham's law of diffusion which governs the diffusion process of gas mixtures [23]:

$$\sum_i N_i \sqrt{M_i} = 0 \tag{20}$$

The molar fluxes of all other non-reacting species are equal to zero [5]. Finally, the relationship between the concentration overpotential and the partial pressures can be written as [31]

- For SOFC–O:

$$\varphi_{conc,an} = \frac{\bar{R}T}{2F} \ln\left(\frac{p_{H_2}^{TPB} p_{H_2O}}{p_{H_2} p_{H_2O}^{TPB}}\right) \tag{21a}$$

$$\varphi_{conc,ca} = \frac{\bar{R}T}{4F} \ln\left(\frac{p_{O_2}}{p_{O_2}^{TPB}}\right) \tag{21b}$$

- For SOFC–H:

$$\varphi_{conc,an} = \frac{\bar{R}T}{2F} \ln\left(\frac{p_{H_2}}{p_{H_2}^{TPB}}\right) \tag{21c}$$

$$\varphi_{conc,ca} = \frac{\bar{R}T}{2F} \ln\left(\frac{p_{H_2O}^{TPB}\sqrt{p_{O_2}}}{p_{H_2O}\sqrt{p_{O_2}^{TPB}}}\right) \tag{21d}$$

3.4. Fuel and oxidant utilization

The utilization of ammonia or urea can be defined in terms of the actual supply and consumption of the fuel or its hydrogen equivalent such that

$$U_f = \frac{(\text{Fuel})_{\text{consumed}}}{(\text{Fuel})_{\text{supplied}}} = \frac{(H_2)_{\text{consumed}}}{(H_2)_{\text{supplied}}} \tag{22}$$

Similarly, the utilization of air as an oxidant can be expressed as a function of the air supply and usage or its oxygen equivalent since air can be assumed to be composed of 79% nitrogen and 21% oxygen by volume.

$$U_o = \frac{(\text{Air})_{\text{consumed}}}{(\text{Air})_{\text{supplied}}} = \frac{(O_2)_{\text{consumed}}}{(O_2)_{\text{supplied}}} \tag{23}$$

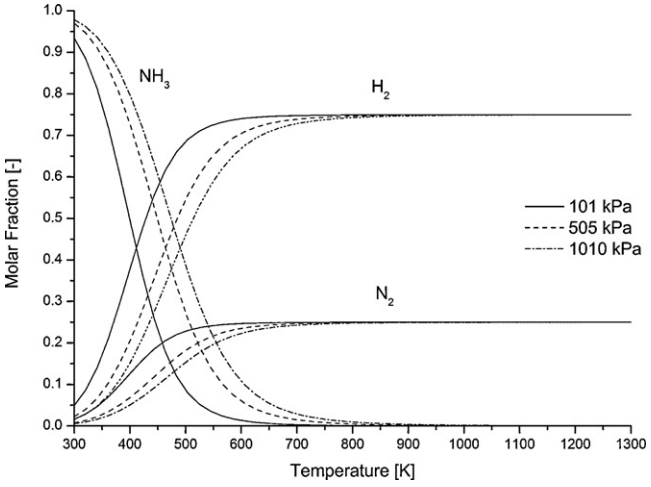

Fig. 3. Thermodynamic equilibrium of ammonia.

4. Results and discussion

In order to obtain the molar fractions and partial pressures of the reacting species at TPB, a computer code has been developed using function (ode45) in MATLAB (MathWorks, Natick, MA, USA) [32] to numerically solve the set of simultaneous differential equations represented by Eq. (11). The required thermodynamic data were obtained from the JANAF tables [33]. The minimization of Eq. (5) was performed using the optimization function in MATLAB.

4.1. Thermolysis of ammonia in DA-SOFC

The use of the GEM method revealed that the decomposition of ammonia is favoured at high temperature and low pressure as shown in Fig. 3. In particular, full conversion of ammonia can be achieved at a temperature of 700 K and atmospheric pressure. Nonetheless, it is well known that the kinetic rate of reaction is rather slow and often requires the use of a suitable catalyst to promote efficient conversion of ammonia. Complete conversion may be achieved over expensive metal catalysts such as ruthenium and platinum at temperatures around 600–650 K [34]; however, more economic alternatives include iron and nickel-based catalysts. Since the operating temperature of solid oxide fuel cells commonly ranges between 900 and 1400 K [35], it is safe to neglect the kinetic rate of reaction and assume that full decomposition of ammonia is attained within the porous anode layer of the fuel cell.

4.2. Reversible cell potential (open cell voltage)

Fig. 4 illustrates the variation of the molar fraction of hydrogen as a function of ammonia utilization at temperature of 1073 K and atmospheric pressure. At the anode of SOFC–O, hydrogen is balanced by the equimolar formation of water vapour due to the electrochemical reaction which results in a linear profile of the hydrogen molar fraction. For SOFC–O, a non-linear profile is observed mainly due to the decomposition of ammonia and consumption of hydrogen.

Fig. 5 shows that the molar fraction of water vapour at the cathode of SOFC–O is higher than that at the anode of SOFC–H at any ammonia utilization factor above 13%. This profile is observed due to the production of water vapour in quantity equal to the hydrogen consumption at the anode of SOFC–O. Conversely, the constant molar fraction of water vapour formation at the cathode of SOFC–H is dependent solely on the invariant oxidant utilization.

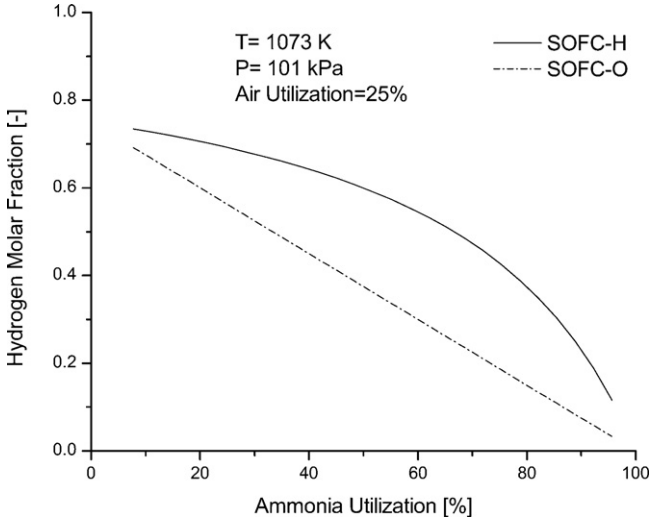

Fig. 4. Molar fraction of hydrogen in DA-SOFC.

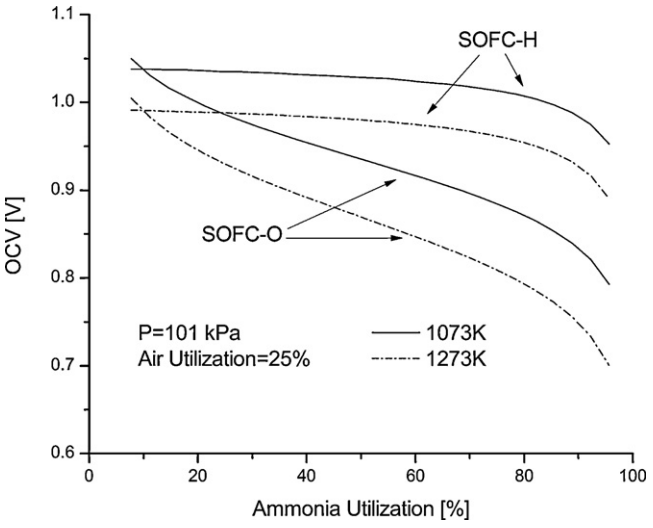

Fig. 6. Open cell voltage of DA-SOFC at different temperatures.

It is always desirable to have a high fuel utilization to maximize the system efficiency; however, high open cell voltage (OCV) is a competing objective which tends to decline as the fuel utilization is increased. Fig. 6 exhibits the OCV of SOFC–O and SOFC–H as a function of fuel utilization. It can be seen that the difference becomes more pronounced at higher fuel utilizations due to the depletion of hydrogen and formation of water vapour.

It is also worth noting that the prediction of OCV values in this study is consistent with the experimental findings of Fuerte et al. [36] who measured the voltage of SOFC–O fuelled with hydrogen and ammonia at temperatures of 973–1173 K. Fig. 7 shows the OCV degradation of both hydrogen and ammonia-fed fuel cells as the operating temperature of the cell increases which also indicates that the reaction mechanisms of both cells are similar and limited to the direct electrochemical oxidation of hydrogen.

Fig. 8 indicates that the OCV can be improved by 5–6% when the operating pressure is increased by five times the atmospheric pressure. This modest enhancement is of particular benefit when the fuel cell is integrated with gas turbine systems (SOFC/GT).

In addition, increasing the air utilization reduces the OCV as shown in Fig. 9. The deterioration is more pronounced in SOFC–H due to higher partial pressure of water vapour and lower partial pressure of oxygen at the cathode.

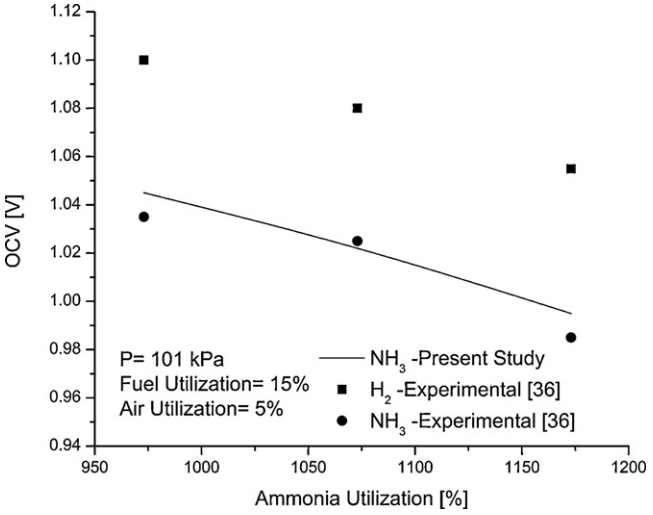

Fig. 7. Comparison of predicted open cell voltage with experimental data (SOFC–O).

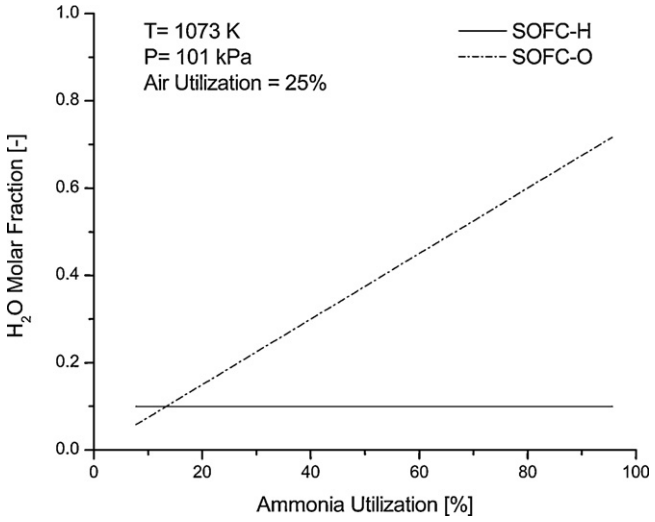

Fig. 5. Molar fraction of water vapour in DA-SOFC.

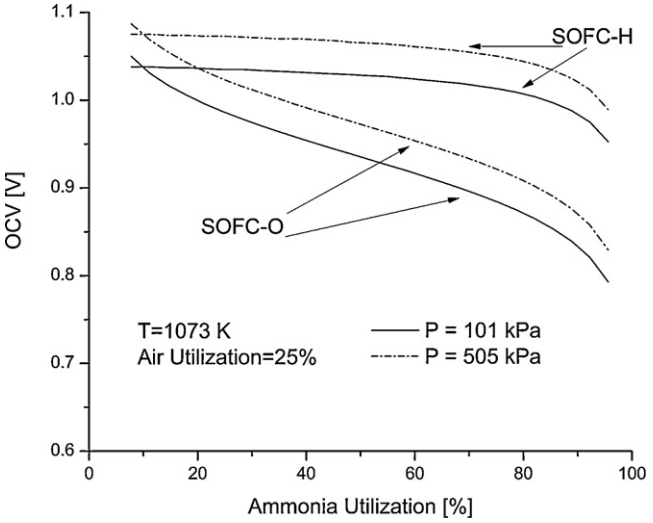

Fig. 8. Effect of pressure on the open cell voltage of DA-SOFC.

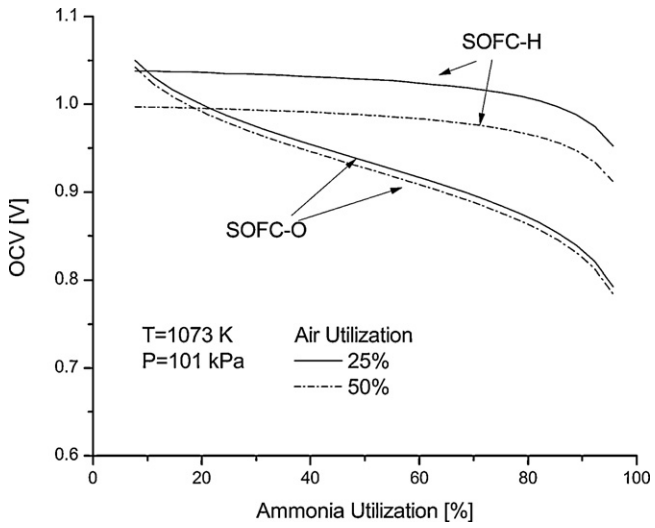

Fig. 9. Effect of oxidant (air) utilization on the open cell voltage of DA-SOFC.

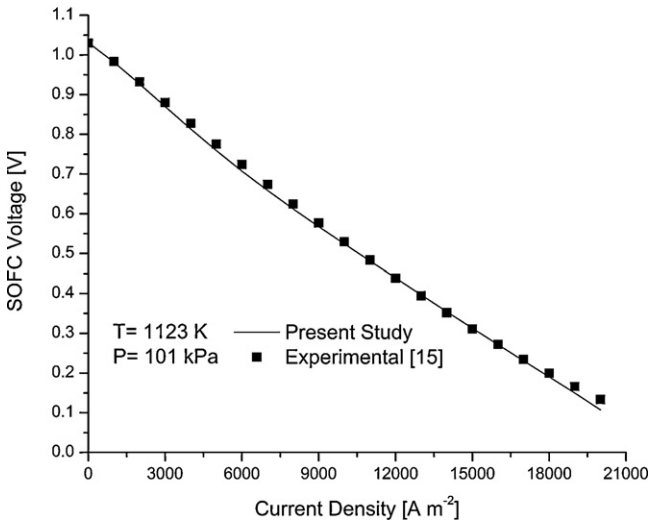

Fig. 10. Comparison of simulation and experimental results of ammonia-fed SOFC–O.

4.3. Operational voltage and performance

4.3.1. Model validation

In the open literature, experimental investigations on ammonia-fed solid oxide fuel cells are scarce and rarely contain all the necessary information and parameters needed for model evaluation. Therefore, certain assumptions were made and some model parameters were adjusted to agree with the experimental data as reflected in Table 2. Ma et al. [15] conducted an experiment in which ammonia was used as a fuel in anode-supported SOFC–O with the arrangement of Ni-YSZ|YSZ|LSM-YSZ. The cell was tested at atmospheric pressure and different temperatures between 923 K and 1123 K. It is worth noting that experimental tests are typically performed with low utilization of reactants in order to avoid the risk of local overheating and degradation which can occur at high current densities. In practice, higher utilization factors are always desirable despite the lower efficiency and specific power output of the fuel cell stack.

In addition, the performance of the cell was characterized by the high interfacial resistance which accounted for about 50% of the total resistance of the cell. The resistance of the electrolyte was also higher than expected at the same temperature as reported elsewhere [31,37]. In part, this can be attributed to the poor contact between the electrodes and the electrolyte as well as the microstructural properties of the cell components which are highly dependent on the processing method as discussed by Ringuedé et al. [38]. The results in Fig. 10 show excellent agreement (within 2%) between the numerical simulation and the experimental data.

4.3.2. Comparison of ion and proton-conducting DA-SOFC

Certain modelling parameters have been fixed to establish a common basis of comparison. The parameters for oxygen ion and proton-conducting DA-SOFC are listed in Table 3. Fig. 11 shows the polarization curve of DA-SOFC operating at 1073 K and atmospheric pressure. It can be seen that high current density can be achieved by employing an anode-supported arrangement of the fuel cell. This can effectively decrease the ohmic over-potential due to the reduction in the electrolyte thickness. The peak power density of SOFC–H is about 21% higher than that of SOFC–O. In addition, the voltage decreases rapidly for both types of fuel cells at high current densities due to the low concentrations of reactants at TPB.

Table 2
Parameters used in the validation of ion-conducting DA-SOFC.

Parameters	Values
Operating temperature, T (K)	1123
Operating pressure, P (kPa)	101
Fuel utilization, U_f (%)	5
Oxidant (air) utilization, U_o (%)	5
Exchange current density of anode, J_{an} (A m^{-2})	$7\times10^9\left(\frac{P_{H_2}}{p^0}\right)\left(\frac{P_{H_2O}}{p^0}\right)\exp\left(-\frac{100{,}000}{RT}\right)$
Exchange current density of cathode, J_{ca} (A m^{-2})	$7\times10^9\left(\frac{P_{O_2}}{p^0}\right)^{0.25}\exp\left(-\frac{130{,}000}{RT}\right)$
Electrode porosity, ε	0.4
Electrode tortuosity, τ	4.25
Average pore radius of electrode, r_p (μm)	0.5
Resistivity of electrolyte, R_Ω (Ω m)	0.735
Anode thickness (μm)	500
Electrolyte thickness (μm)	30
Cathode thickness (μm)	10

Sources: [8,15,39,40].

Table 3
Parameters used in modelling the polarization curve of DA-SOFC.

Parameters	Values
Fuel utilization, U_f (%)	5
Oxidant utilization, U_o (%)	5
Exchange current density of anode |SOFC–O, J_{an} (A m^{-2})	$7\times10^9\left(\frac{P_{H_2}}{p^0}\right)\left(\frac{P_{H_2O}}{p^0}\right)\exp\left(-\frac{100000}{RT}\right)$
Exchange current density of cathode |SOFC–O, J_{ca} (A m^{-2})	$7\times10^9\left(\frac{P_{O_2}}{p^0}\right)^{0.25}\exp\left(-\frac{130000}{RT}\right)$
Exchange current density of anode |SOFC–H, J_{an} (A m^{-2})	2500@1073 K 5000@1273 K
Exchange current density of cathode |SOFC–H, J_{ca} (A m^{-2})	1700@1073 K 3400@1273 K
Electrode porosity, ε	0.4
Electrode tortuosity, τ	4.25
Average pore radius of electrode, r_p (μm)	0.5
Resistivity of electrolyte |SOFC–O, R_Ω (Ω m)	$2.94\times10^{-5}\exp\left(\frac{10350}{T}\right)$
Resistivity of electrolyte |SOFC–H, R_Ω (Ω m)	0.37@1073 K 0.21@1273 K
Anode thickness (μm)	500
Electrolyte thickness (μm)	30
Cathode thickness (μm)	30

Sources: [8,15,37,39–42].

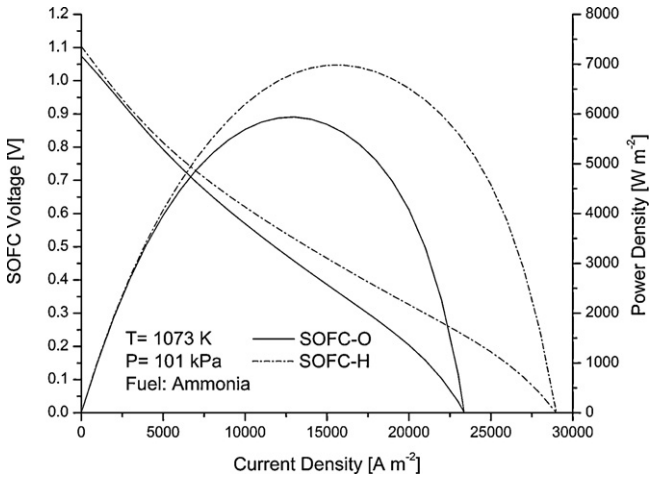

Fig. 11. Polarization curve of DA-SOFC at 1073 K and atmospheric pressure.

As depicted in Fig. 12, the activation over-potentials of SOFC–O and SOFC–H anodes are comparable; however, it is rather higher at the cathode of SOFC–H in comparison to that at the cathode of its counterpart. This is highly affected by the difference in exchange current density which is estimated to be about 2200 A m^{-2} for SOFC–O and 1700 A m^{-2} for SOFC–H at the given temperature and pressure. The effect of higher activation over-potential in SOFC–H is compensated by the low ohmic over-potential as shown in Fig. 13. The resistivity (or ionic conductivity) of electrolyte is highly influenced by the chemical composition, processing method and sintering temperature [38]. The values of resistivity used in this numerical study are 0.455 Ω m [43] for oxygen ion-conducting electrolyte (YSZ) and 0.370 Ω m [39] for proton-conducting barium cerate neodymium oxide (BCNO) electrolyte at 1073 K and represent an average of the values found in the literature.

Fig. 14 reflects the effect of concentration over-potential on the performance of anode-supported DA-SOFC. Due to the thickness of the anode, its concentration over-potential is significantly higher than that of the cathode. Moreover, the over-potential is more pronounced at the anode of SOFC–O due to the formation of water vapour at the anode–electrolyte interface and its diffusion through the porous anode into the gas channel.

Additionally, the operating temperature has a major impact on the performance of the fuel cell. Fig. 15 demonstrates the increase in power density despite the slight decrease in OCV caused by the increase in operating temperature from 1073 to 1273 K. The higher operating voltage and current density are the result of lower over-potentials at high temperatures. The peak power density of SOFC–O is about 50% higher than that of SOFC–H which is mainly due to the

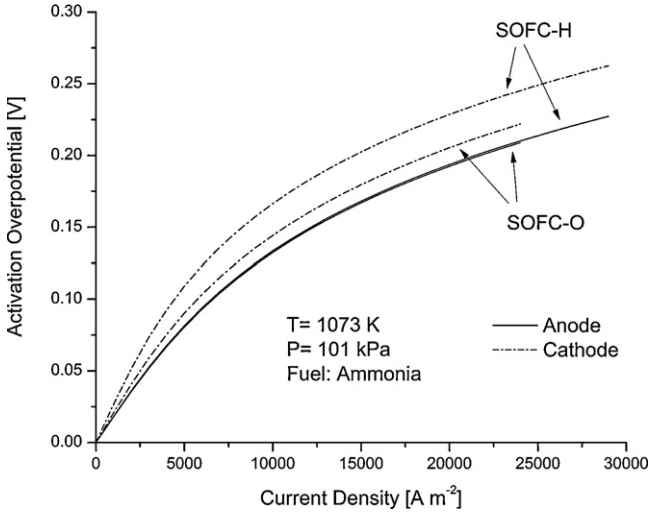

Fig. 12. Activation over-potential of anode-supported DA-SOFC.

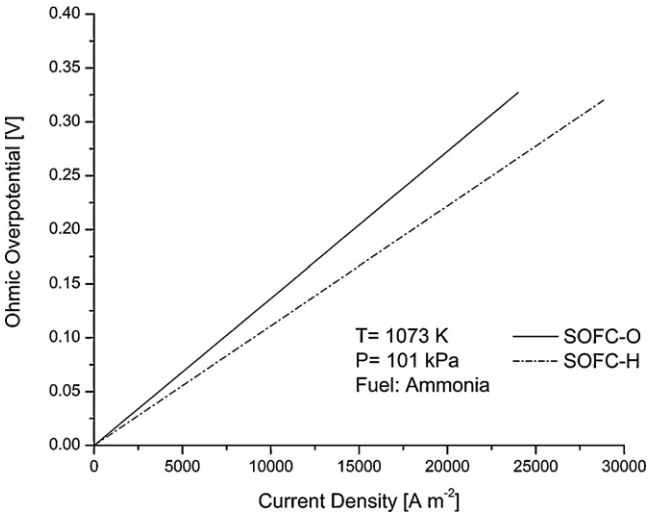

Fig. 13. Ohmic over-potential of anode-supported DA-SOFC.

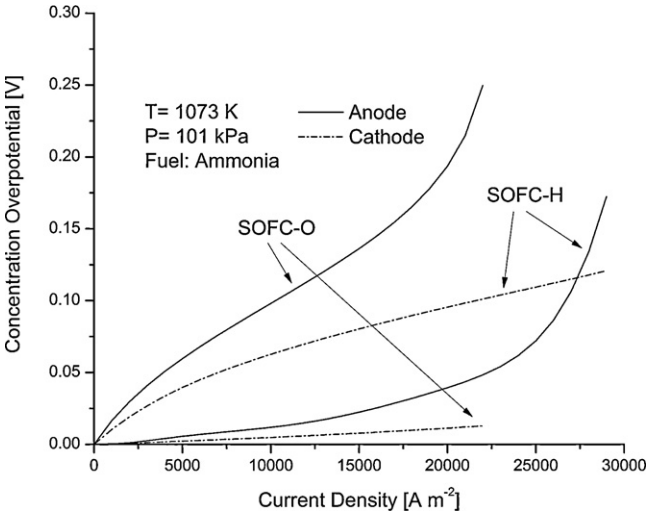

Fig. 14. Concentration over-potential of anode-supported DA-SOFC.

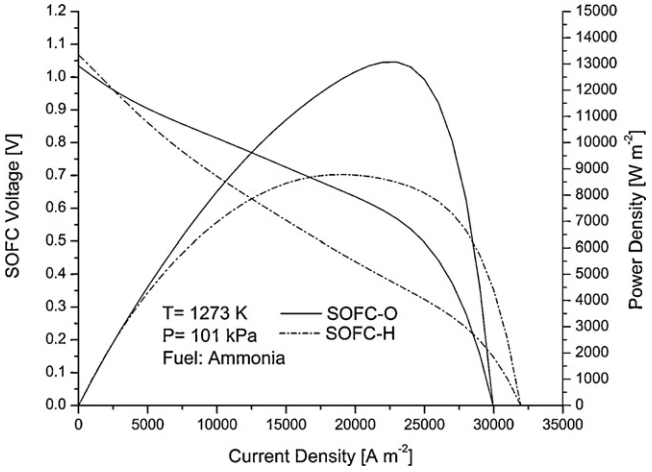

Fig. 15. Polarization curve of DA-SOFC at 1273 K and atmospheric pressure.

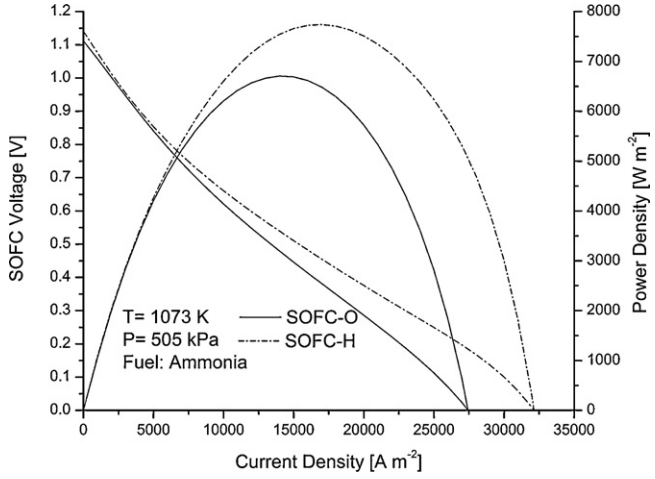

Fig. 16. Polarization curve of DA-SOFC at 1073 K and pressure of 505 kPa.

uncertainty in estimating the exchange current density of SOFC–H in contrast to the rate expression used for SOFC–O counterpart. The difference in peak power density obtained in this study may be somewhat justified by recognizing that the performance of SOFC–H deteriorates at elevated temperatures due to the high electronic conductivity of the electrolyte as given by various accounts in the literature (e.g. [39,42]). Therefore, it is highly discouraged to utilize and operate SOFC–H cells at temperatures beyond 1073 K.

Finally, Fig. 16 illustrates the increase in the power density of the fuel cell at elevated operating pressure. The performance improvement is the result of a slight increase in OCV and moderate enhancement of the permeation of gaseous species to and from the reaction sites at TPB.

5. Conclusions

The merits of using ammonia as a hydrogen carrier have been highlighted in this study. The operating principles of ammonia-fed solid oxide fuel cells have been illustrated as well. In order to investigate the cell-level thermodynamic and electrochemical performances at open and closed circuit conditions, a model was developed and validated by excellent agreement with experimental data obtained from the literature.

Furthermore, the parametric analyses performed in this work revealed that proton-conducting DA-SOFC maintained higher reversible cell potential than the ion-conducting counterpart under all open-circuit conditions. Under closed-circuit conditions, the proton-conducting DA-SOFC demonstrated a better performance in comparison to the ion-conducting counterpart due to higher partial pressure of hydrogen at the anode under all operating conditions.

The results of this work emphasized the advantages of the operating principle and performance of SOFC–H; however, their performance is highly influenced by many factors such as the type of electrolyte used and the microstructural properties of the electrodes. As such, all design parameter must be optimized to achieve the best possible performance.

References

[1] A. Klerke, C.H. Christensen, J.K. Nørskov, T. Vegge, Journal of Materials Chemistry 18 (2008) 2304–2310.
[2] T.B. Marder, Angewandte Chemie—International Edition 46 (2007) 8116–8118.
[3] M. Ni, D.Y.C. Leung, M.K.H. Leung, Journal of Power Sources 183 (2008) 682–686.
[4] A. Demin, P. Tsiakaras, International Journal of Hydrogen Energy 26 (2001) 1103–1108.
[5] M. Ni, D.Y.C. Leung, M.K.H. Leung, International Journal of Hydrogen Energy 33 (2008) 5765–5772.
[6] S. Assabumrungrat, W. Sangtongkitcharoen, N. Laosiripojana, A. Arpornwichanop, S. Charojrochkul, P. Praserthdam, Journal of Power Sources 148 (2005) 18–23.
[7] P.M. Biesheuvel, J.J.C. Geerlings, Journal of Power Sources 185 (2008) 1162–1167.
[8] M. Ni, D.Y.C. Leung, M.K.H. Leung, Journal of Power Sources 183 (2008) 687–692.
[9] M. Ni, D.Y.C. Leung, M.K.H. Leung, Journal of Power Sources 185 (2008) 233–240.
[10] A.S. Chellappa, C.M. Fischer, W.J. Thomson, Applied Catalysis A: General 227 (2002) 231–240.
[11] Chemical Industry News & Intelligence (November, 2010), Ammonia Uses and Market Data 2010, http://www.icis.com/v2/chemicals/9075154/ammonia/uses.html.
[12] European Fertilizer Manufacturers' Association (November, 2010), Production of Ammonia, BAT Booklet, 2000, http://www.efma.org/documents/file/bat/BAT%20Production%20of%20Ammonia.pdf.
[13] U.S. Department of Energy (November, 2010), Status of Hydrogen Storage Technologies, http://www1.eere.energy.gov/hydrogenandfuelcells/storage/tech_status.html.
[14] Canadian Centre for Occupational Health and Safety (December, 2010), Working Safely with Ammonia Gas, 2003, http://www.ccohs.ca/oshanswers/chemicals/chem_profiles/ammonia/working_ammonia.html.
[15] Q. Ma, J. Ma, S. Zhou, R. Yan, J. Gao, G. Meng, Journal of Power Sources 164 (2007) 86–89.
[16] NIST (October, 2010), Thermophysical Properties of Hydrogen, http://webbook.nist.gov/cgi/fluid.cgi?ID=C1333740&Action=Page.
[17] Wisconsin Department of Health Services (October, 2010), Summary of Ammonia Accidents in the United States to Which OSHA Responded, http://www.dhs.wisconsin.gov/eh/hsees/PDFfiles/AmmoniaAccidentSumm.pdf.
[18] C.H. Christensen, R.Z. Sørensen, T. Johannessen, U.J. Quaade, K. Honkala, T.D. Elmøe, R. Køhler, J.K. Nørskov, Journal of Materials Chemistry 15 (2005) 4106–4108.
[19] M.M. Mench, Fuel Cell Engines, John Wiley & Sons, Hoboken, NJ, 2008, pp. xi 515.
[20] M. Ni, D.Y.C. Leung, M.K.H. Leung, Energy Conversion and Management 50 (2009) 268–278.
[21] A. Arpornwichanop, Y. Patcharavorachot, S. Assabumrungrat, Chemical Engineering Science 65 (2010) 581–589.
[22] S.H. Chan, C.F. Low, O.L. Ding, Journal of Power Sources 103 (2002) 188–200.
[23] R. Suwanwarangkul, E. Croiset, M.W. Fowler, P.L. Douglas, E. Entchev, M.A. Douglas, Journal of Power Sources 122 (2003) 9–18.
[24] V. Janardhanan, A detailed approach to model transport, heterogeneous chemistry, and electrochemistry in solid-oxide fuel cells, Universitätsverlag, Karlsruhe, PhD Thesis, ISBN: 978-3-86644-184-2, 2007.
[25] C.K. Ho, S.W. Webb, Gas Transport in Porous Media, Springer, Dordrecht, 2006.
[26] R.B. Bird, E.N. Lightfoot, W.E. Stewart, Transport Phenomena, 2nd ed., John Wiley, New York/Toronto, 2002.
[27] B.E. Poling, J.M. Prausnitz, J.P. O'Connell, The Properties of Gases and Liquids, 5th ed., McGraw-Hill, New York, 2001.
[28] H. Zhu, R.J. Kee, V.M. Janardhanan, O. Deutschmann, D.G. Goodwin, Journal of the Electrochemical Society 152 (2005) A2427–A2440.
[29] N.J. Themelis, Transport and Chemical Rate Phenomena, Gordon and Breach Publishers, Basel, Switzerland, 1995.
[30] H. Zhu, R.J. Kee, Journal of Power Sources 117 (2003) 61–74.
[31] Y. Patcharavorachot, W. Paengjuntuek, S. Assabumrungrat, A. Arpornwichanop, International Journal of Hydrogen Energy 35 (2010) 4301–4310.
[32] MathWorks Inc., MATLAB, Version 7.5, Natick, MA, USA, 2007.
[33] M.W. Chase, NIST-JANAF Thermochemical Tables, 4th ed., American Institute of Physics for the National Institute of Standards and Technology, New York, 1998.
[34] R.Y. Chein, Y.C. Chen, C.S. Chang, J.N. Chung, International Journal of Hydrogen Energy 35 (2010) 589–597.
[35] EG & G. Services, Fuel Cell Handbook, U.S. Dept. of Energy, Office of Fossil Energy, National Energy Technology Laboratory, Morgantown, WV, 2004.
[36] A. Fuerte, R.X. Valenzuela, M.J. Escudero, L. Daza, Journal of Power Sources 192 (2009) 170–174.
[37] P.W. Li, M.K. Chyu, Journal of Heat Transfer 127 (2005) 1344–1362.
[38] A. Ringuedé, D. Bronine, J.R. Frade, Solid State Ionics 146 (2002) 219–224.
[39] K. Xie, Q. Ma, B. Lin, Y. Jiang, J. Gao, X. Liu, G. Meng, Journal of Power Sources 170 (2007) 38–41.
[40] A.V. Akkaya, International Journal of Energy Research 31 (2007) 79–98.
[41] F. Chen, P. Wang, O. Toft Sørensen, G. Meng, D. Peng, Journal of Materials Chemistry 7 (1997) 1533–1539.
[42] L. Zhang, W. Yang, Journal of Power Sources 179 (2008) 92–95.
[43] C. Bo, C. Yuan, X. Zhao, C.B. Wu, M.Q. Li, Clean Technologies and Environmental Policy 11 (2009) 391–399.